GaP-ZnS Multilayer Films: Visible-Light Photoelectrodes by Interface Engineering

Collin K. Park[1], Paria S. M. Gharavi[1], Fran Kurnia[1,†], Qi Zhang[1], Cui Ying Toe[2], Mohammed Al-Farsi[1], N. L. Allan[3], Yin Yao[4], Lin Xie[5], Jiaqing He[5], Yun Hau Ng[2], Nagarajan Valanoor[1,], and Judy N. Hart[1,]**

[1]School of Materials Science and Engineering, UNSW Sydney, NSW 2052, Australia
*E-mail: nagarajan@unsw.edu.au or j.hart@unsw.edu.au

[2]Particles and Catalysis Research Group, School of Chemical Engineering, UNSW Sydney, NSW 2052, Australia

[3]School of Chemistry, University of Bristol, Cantock's Close, Bristol, BS8 1TS, UK

[4]Electron Microscope Unit, Mark Wainwright Analytical Centre, UNSW Sydney, NSW 2052, Australia

[5]Department of Physics, Southern University of Science and Technology (SUSTech), Shenzhen 518055, China.

[†] Current address: Centre for Nanostructured Media, School of Mathematics and Physics, Queen's University Belfast, Belfast, Northern Ireland BT7 1NN, UK.

ABSTRACT

In the field of solar water splitting, searching for and modifying bulk compositions has been the conventional approach to enhancing visible-light activity. In this work, manipulation of heterointerfaces in ZnS-GaP multilayer films is demonstrated as a successful alternative approach to achieving visible-light-active photoelectrodes. The photocurrent measured under visible light increases with increasing number of interfaces for ZnS-GaP multilayer films with the same total thickness, indicating it to be a predominantly interface-driven effect. The activity extends to long wavelengths (650 nm), much longer than expected for pure ZnS, and also longer than previously reported for GaP. Density functional theory (DFT) calculations of ZnS-GaP multilayers predict the presence of electronic states associated with atoms at the interfaces between ZnS and GaP that are different from those found within the layers away from the interfaces; these states, formed due to unique bonding environments found at the interfaces, lead to a lowering of the band gap and hence the observed visible-light activity. The presence of these electronic states attributed to the interfaces is confirmed by depth-resolved X-ray photoelectron spectroscopy. Thus, we show that interface engineering is a promising route for overcoming common deficiencies of individual bulk materials caused by both wide band gaps and indirect band gaps, and hence enhancing visible-light absorption and photoelectrochemical performance.

1. INTRODUCTION

Achieving high solar-to-hydrogen conversion efficiencies for photoelectrochemical (PEC) water splitting requires a semiconductor with a combination of properties that has proved difficult to achieve with a single bulk material.[1,2] In particular, many of the popularly studied binary metal oxide semiconductors have wide band gaps (> 3 eV), including TiO_2, $SrTiO_3$ and ZnO.[1,3] This is an inherent limitation of oxides, at least for cation electron configurations of d^0 and d^{10}, due to the highly positive potential of the valence bands formed by O 2p states.[4,5] A practical implication of such wide band gaps is that light absorption is only possible at UV wavelengths. However, 43% of the energy in sunlight (AM1.5) is in the visible range (400 nm < λ <700 nm), meaning that the solar conversion efficiencies of wide band gap materials are severely limited.[6,7] Thus, developing photoactive materials, particularly non-oxides, that can absorb visible light is critical to achieving high efficiencies. In order to achieve practical efficiencies, it has been proposed that photoactivity must be extended to a wavelength of at least 600 nm.[1,4]

This has necessitated materials development strategies to enhance visible-light absorption. Popular approaches have often focused on modification of bulk composition, such as doping[1,8-10] and element substitution.[11] Manipulating interfaces[12] in thin film structures, on the other hand, is a relatively unexplored approach that provides alternative opportunities for controlling electronic properties and hence light absorption behavior. Modern thin film synthesis techniques allow materials with starkly contrasting properties to be combined into composite structures with atomic-level control.[13,14] The underlying principle of using such composite thin film structures (e.g. multilayered films) is that the imposed proximity and two-dimensional constraint between the two contrasting materials can create physicochemical conditions at the heterointerfaces that lead to atomic bonding environments and hence electronic states that are not present in either bulk material on its own.

While heterointerfaces have been widely used in photocatalysis and photovoltaic devices to improve charge separation,[15-18] here we show that interface engineering (as opposed to modifying bulk compositions) can also be successfully exploited to enhance visible-light absorption and hence improve PEC performance, and can result in visible-light activity that greatly exceeds the performance of the individual materials.

The model system used in this work is a new non-oxide material system – ZnS-GaP multilayered films. While photoelectrode materials are predominantly oxides, recent reports of non-oxide semiconductors for PEC water splitting have included GaP nanowires,[19] a Cu_3BiS_3 photocathode (found to have an indirect band gap of 1.6 eV and able to reach a photocurrent of ~10 μA/cm^2 under AM 1.5G simulated solar radiation),[20] and a monolithic GaInP/GaInAs dual-absorber tandem device.[21] These non-oxide materials often have poor stability in contact with electrolytes and require protective layers.[22,23]

The choice of ZnS and GaP in this work was based on theoretical predictions that direct band gaps close to the optimum value of 2.0 eV are readily achievable in this material system.[24] Pure ZnS itself has a wide band gap of 3.6 eV, so should be inactive at visible-light wavelengths. Pure GaP has a band gap of 2.3 eV, but the indirect nature of the band gap leads to light absorption depths much greater than the minority-carrier diffusion length, and hence low photocurrents.[19,25] Our previous theoretical work[24] showed that the addition of ZnS to GaP converts the band gap from indirect to direct. ZnS and GaP have very similar lattice parameters (<1% mismatch), allowing ready mixing. Slight incorporation of GaP into ZnS nanowires has shown enhancement in photocurrent magnitude and stability.[26] Similar systems of mixed semiconductors have shown good visible-light photocatalytic activity; for example, a high efficiency for visible-light photocatalysis (5.9% quantum yield at 420 – 440 nm without sacrificial agents) has been reported.[27]

2. EXPERIMENTAL AND COMPUTATIONAL METHODS

Film fabrication. ZnS and GaP films were deposited on silicon (1 0 0) substrates by pulsed laser deposition (PLD) using a KrF excimer laser (λ = 248 nm, 20 ns pulse duration). The substrates were heated to 500^{o}C under vacuum (base pressure: 10^{-8} Torr) before film deposition. ZnS and GaP ceramic targets were ablated alternatively using an automatic looping code in LabView 2013 to create the multilayer structures. After film deposition, the samples were cooled to room temperature at a rate of 10^{o}C/min. The crystal structures were determined by θ-2θ X-ray diffraction analysis using an Empyrean X-ray diffractometer (X'pert, Panalytical).

Characterization. Cross-sectional transmission electron microscope (TEM) specimens were prepared by mechanical polishing followed by argon ion thinning at 1-3 kV using a precision ion polishing system (PIPS, i.e. cutting, grinding, dimpling, polishing) followed by Ar-ion

milling with a liquid nitrogen cooling stage. We employed a double Cs corrected scanning transmission electron microscopy (STEM) to study chemical composition and measure the thickness of the ZG multilayer film. Scanning-TEM/TEM investigations were carried out in a Tecnai F30 and double aberration corrected Titan Cubed Themis G2 300 TEM operated at 300 kV. Energy dispersive spectroscopy (EDS) was performed using a double aberration corrected Titan Cubed Themis G2 300 TEM operated at a voltage of 200 kV. All quantification results presented in this work have been calculated with Digital Micrograph software (DM, Gatan Inc., US). The surface morphology of the multilayer films was analyzed by a commercial atomic force microscope (AFM, Cypher, Asylum Research, US).

UV-visible spectra were acquired with a Lambda 950 UV/vis/NIR spectrophotometer over a wavelength range of $250 - 800$ nm. The films used for UV-visible spectroscopy were deposited on quartz substrates, to allow measurement in transmission mode to minimize interference effects.

Depth-resolved X-ray photoelectron spectroscopy **(XPS).** The chemical state of the ions in the Z/G-4 sample was investigated by depth-resolved XPS. The measurements were carried out on a Thermo Scientific ESCALAB 250Xi under vacuum ($< 2 \times 10^{-9}$ mbar), using a monochromatic Al Kα source 1486.68 eV, with a spectral resolution of 800 meV. The sample was etched with an Ar ion beam at an energy of 1 keV.

Photoelectrochemical performance. PEC measurements were carried out in 0.1 M H_2SO_4 electrolyte solution at room temperature in a standard three-electrode configuration with Pt as the counter electrode, Ag/AgCl as the reference electrode, and the multilayer film as the working electrode. Linear sweep voltammetry (LSV) measurements were made under intermittent ON-OFF illumination at a scan rate of 100 mV/s, with the potential applied by an Autolab potentiostat (PGSTAT302N) over the range −1.0 V to 1.0 V. A cut-off filter was used to obtain light of wavelength $\lambda \geq 435$ nm from a 300 W Xe lamp (Oriel). A bias of 0.2 V was used for acquiring the action spectra.

Density functional theory (DFT) Calculations. The DFT method has been described previously.[24] Briefly, the electronic properties of a ZnS/GaP multilayered structure were calculated with the CRYSTAL14 code,[28,29] using an 86-4111(d41) basis set for Zn,[30] an 86-311(d) basis set for S,[31] and pseudopotentials for Ga and P.[32] Basis set parameters for the

valence functions were re-optimized for GaP and ZnS. The B3PW hybrid method[33,34] was used with 15% Hartree-Fock exchange energy mixed with the DFT exchange-correlation energy. The Monkhorst-Pack grid for *k*-points sampling of the Brillouin zone was set to 12 × 12 × 12. The electronic density of states (DOS) was calculated for a periodic structure consisting of alternating layers of ZnS and GaP, where the crystallographic plane of the interface was (111) (to match the preferred growth direction of ZnS determined by XRD). Each layer had a thickness of 3 atomic bilayers (where each bilayer consists of one layer of cations and one layer of anions), giving a total of 6 atomic bilayers, and 12 atoms, in the supercell. The dimensions of the supercell in the directions perpendicular to the interface were 3.92 Å × 3.92 Å. The DOS was calculated after a full geometry optimization of all atomic positions and lattice parameters. The thresholds for convergence of the maximum gradient, RMS gradient, maximum displacement and RMS displacement were 4.5×10^{-4}, 3.0×10^{-4}, 1.8×10^{-3} and 1.2×10^{-3} a.u., respectively.

3. RESULTS AND DISCUSSION

The structures of the multilayer films deposited by pulsed laser deposition (PLD) are shown in Figure 1a. The films consist of alternating ZnS and GaP layers with different numbers of ZnS/GaP (Z/G) interfaces. Hereafter, we label the films as "Z/G-*x*" where *x* is the number of interfaces in the multilayer structure. The overall thickness of each film is similar (~300 nm, Supporting Information Figure S1), corresponding to the same total number of laser pulses used for ZnS and GaP deposition. The outer layer of all films is ZnS, to ensure consistency of the surface chemistry and to avoid direct contact between the electrolyte and GaP, which has poor stability[21,35]. Films of only ZnS (labeled "Z") and only GaP (labeled "G") were also deposited for comparison. Topographic atomic force microscopy (AFM) images of the film surfaces show that the surfaces are quite similar in roughness (not shown).

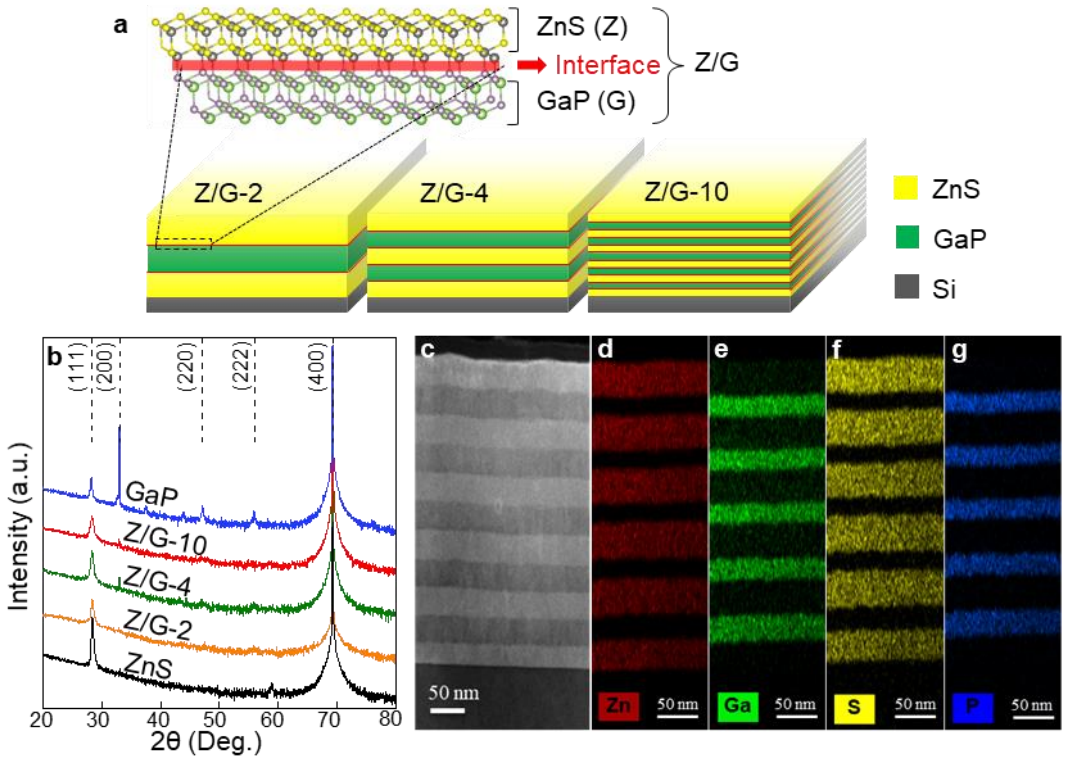

Figure 1. (a) Schematic illustration of the three ZnS-GaP multilayer films with different numbers of interfaces. (b) X-ray diffraction (XRD) patterns of all samples. (c) High-angle annular dark-field (HAADF) cross-section image of Z/G-10 with electron dispersive spectroscopy (EDS) maps of each element (d – Zn, e – Ga, f – S, g – P).

Figure 1b shows the X-ray diffraction (XRD) patterns of the multilayered films. The patterns of all the films show a strong peak at 69.2° attributed to the (400) plane of the silicon substrate, which is a single crystal oriented in the (100) direction. Aside from this silicon peak, the patterns of Z, Z/G-2, Z/G-4, and Z/G-10 only show one prominent peak, assigned to the (111) lattice plane of the cubic zinc blende structure. In contrast, the GaP film shows additional peaks assigned to the (200) (220) and (222) lattice planes, indicating that GaP does not have a preferred growth direction. The 2θ position of the (111) peak for the multilayered films is intermediate between those of pure ZnS and GaP (Supporting Information Figure S2).

Cross-section transmission electron microscopy (TEM) coupled with energy dispersive spectroscopy (EDS) mapping was performed to examine the nature of the interfaces. Figure 1c is a cross-section TEM image of the Z/G-10 sample. The lattice spacing obtained from the selective area electron diffraction pattern (not shown) is consistent with the lattice constant

calculated from the XRD patterns. The high-angle annular dark field (HAADF) STEM image (Figure 1c) reveals each ZnS and GaP layer to be similar in thickness (~ 25 nm). However, the EDS maps (acquired on the same TEM) of the four elements (Figure 1d-g) reveal that the ZnS layers are thicker than the GaP layers. This increased thickness of the ZnS layers arises from a ~ 5 nm interdiffused region at the interfaces where ZnS diffuses into the GaP layers. As a consequence of the interdiffusion, the ZnS-GaP interfaces are not atomically flat but have wavy profiles (as seen in Figure 1c). We are confident this is not due to scanning or TEM sample preparation artefacts, as the ZnS-substrate interface is atomically smooth. Full details of the interfacial structure and interdiffused regions are beyond the scope of the current work and will be reported elsewhere.

UV-visible spectra of all samples are shown in Figure 2a (measured in transmission mode on quartz substrates). As the number of interfaces increases, the band gap slightly decreases. While weak absorption peaks are seen at visible-light wavelengths for the multilayer films, most notably a shoulder peak centred at ~ 420 nm for Z/G-10, it is not clear if these peaks are due to absorption by the films or interference effects. These results indicate that the presence of ZnS/GaP interfaces does not strongly influence the absorption of the bulk material and light absorption is dominated by ZnS.

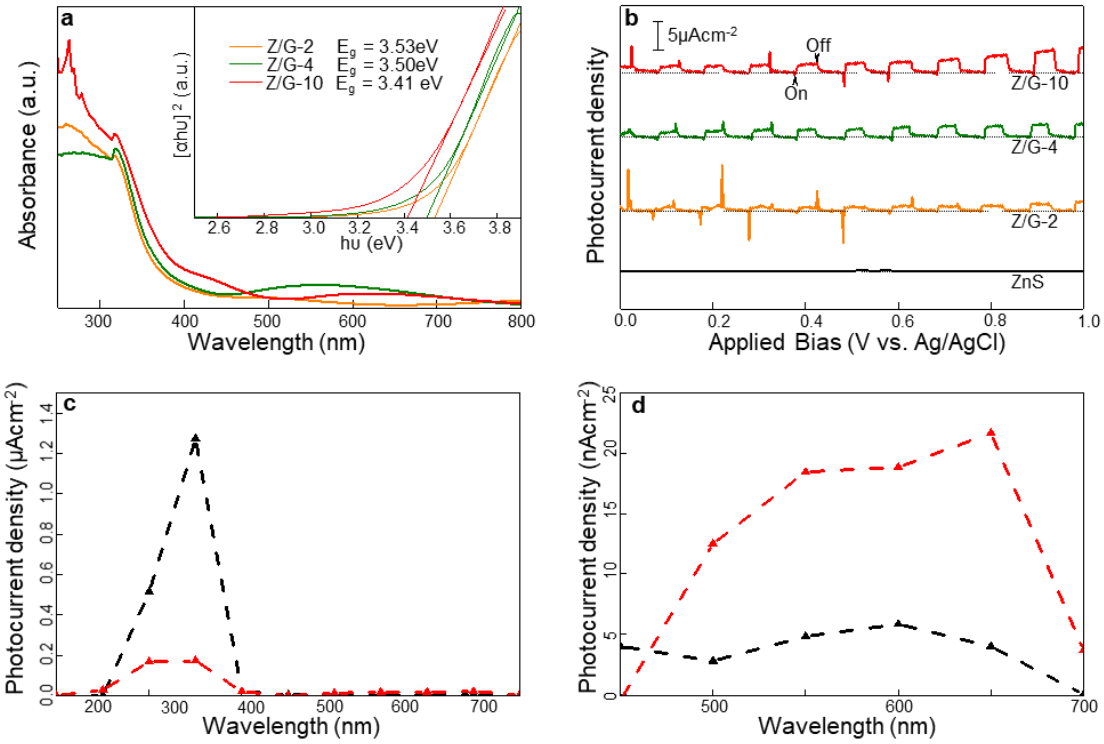

Figure 2. (a) UV-visible spectra of all samples measured in transmission mode; inset shows Tauc plots. (b) Linear sweep voltammograms of the three multilayer films measured under visible-light illumination (λ > 435 nm) from 0 V to 1 V bias. (c) Action spectra for the Z (black dashed line) and Z/G-10 (red dashed line) films, measured at 0.2 V bias. (d) Action spectra for the Z (black dashed line) and Z/G-10 (red dashed line) films at visible-light wavelengths, measured at 0.2 V bias.

Figure 2b shows the photoelectrochemical (PEC) performance of the multilayer films as well as the ZnS film, measured by linear sweep voltammetry (LSV) under intermittent ON-OFF visible-light illumination ($\lambda \geq 435$ nm). All films show *n*-type behavior (data are not shown for the GaP film due to its instability in the electrolyte). It should be noted that the photocurrents are measured under only visible-light irradiation, with no co-catalyst, and the electrolyte is not sacrificial. The photocurrent density for all the multilayer films is significantly higher than for the film of only ZnS, which produces negligible photocurrent. Importantly, it increases with increasing number of ZnS/GaP interfaces, reaching a maximum of 4.4 μA/cm^2 for Z/G-10 at 1.0 V bias. In contrast to many non-oxide semiconductors that

corrode rapidly in direct contact with electrolytes, the films showed good stability over the timescale of the measurement (40 minutes); stability will be further studied in future work.

The action spectra for both the ZnS and Z/G-10 films are shown in Figure 2c and 2d. It can be seen that Z/G-10 shows clear photoactivity under visible-light wavelengths that is significantly higher than the photoactivity of ZnS. The photoactivity for Z/G-10 extends to a wavelength of 650 nm, much longer than expected for pure ZnS, and longer than previously reported for GaP[36,37], the mixed semiconductor system GaN-ZnO[27,38] and most oxide photoelectrodes (*e.g.* TiO_2 even when doped with nitrogen[39] or transition metals[40], and $BiVO_4$[41]).

Since all three films show similar surface morphology, we can eliminate surface roughness as a significant factor. On the other hand, photocurrent density increases with number of interfaces, which suggests that they are predominantly responsible for the visible-light absorption.

To understand how the interfaces in the multilayered films can give enhanced visible-light activity, we performed a density functional theory (DFT) calculation of a ZnS-GaP multilayer structure, shown in Figure 3a. From our previous work, the band gaps of ZnS and GaP calculated using this DFT method are 3.4 eV (direct) and 2.5 eV (indirect), respectively, in good agreement with the experimentally-measured values[42]. The band gap of the multilayer structure is 2.1 eV, smaller than that of either pure ZnS or GaP; the band gap is direct. To investigate the origin of band gap reduction, we calculated the projected densities of states (DOS) for the multilayered structure (Figure 3b). It can be seen that the top of the valence band is formed by states on P atoms at the interface with ZnS and the bottom of the conduction band is formed by states on Ga atoms at the interface with ZnS. Thus, it is the Zn-P and Ga-S bonds at the interfaces between layers that determine the valence and conduction band energies and hence it is the presence of these bonds that causes the band gap reduction. It should be noted that, while the thickness of the ZnS and GaP layers in the structure used for the DFT calculation is much less than that of the synthesized films, DFT calculations for different layer thicknesses have been completed and all lead to the same overall conclusion that the band gap reduction is due to the presence of Zn-P and Ga-S bonds at the interfaces.

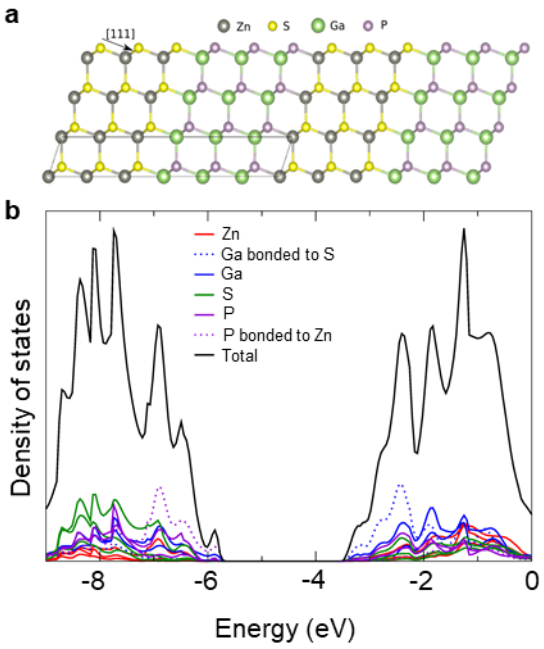

Figure 3. (a) Calculated optimized geometry of the ZnS/GaP multilayer structure used for the DFT calculation; the interfacial plane is (111). The black line shows the boundary of the simulation cell. (b) Projected densities of states for the ZnS/GaP multilayer structure.

The DFT results indicate that there are unique atomic bonding environments at the interfaces (i.e. Zn-P and Ga-S bonds), that give rise to electronic states that are not present in the ZnS and GaP away from the interfaces, and it is these electronic states that reduce the band gap locally at the interfaces. To further confirm the changes in the electronic states at the ZnS-GaP interfaces, we used depth-resolved X-ray photoelectron spectroscopy (XPS) to characterize the binding energies vs. depth through the cross-section of the Z/G-4 film. Figure 4a shows a two-dimensional contour map in the energy region of the Zn 3d and Ga 3d peaks. Figures 4b and 4c show the Zn 3d and Ga 3d peaks, respectively, at the interface closest to the substrate and Figure 4d shows the Ga 3d peak at the 2nd interface from the substrate. The 3d peak positions within the ZnS and GaP layers are in general agreement with the expected values.[43,44] Within the GaP layers, the Ga 3d peak is at 19.2 eV. However, as the interface is approached, the Ga 3d peak gradually becomes asymmetric and develops a shoulder at an energy of ~ 21 eV (indicated by the arrows in Figures 4c and 4d), which may be attributed to Ga bonded to ZnS at the interface. The presence of this peak at the interface at a higher binding than Ga 3d in GaP indicates a lowering of the Ga energy states and hence a lowering of the conduction band energy, consistent with both the DFT results, which show the conduction band minimum is dominated by Ga at the interface (Figure 3b), and the observed

increase in visible-light photocurrent attributed to the interfaces. This same shoulder peak for Ga 3d at a binding energy of ~ 21 eV is also seen at the other two interfaces of the Z/G-4 sample (Supporting Information Figure S3). A similar effect is observed for Zn. The Zn 3d peak within the layer closest to the substrate is seen at a binding energy of 10.8 eV. As the interface with GaP is approached, the Zn 3d peak shifts in energy to 11.2 eV (indicated by the arrow in Figure 4b). This peak shift persists in all the subsequent ZnS layers where there is a trace concentration of Ga. Thus, the shift may be attributed to Zn bonded to GaP and again shows that atomic environments at the interfaces give rise to electronic states not seen in either pure ZnS or GaP.

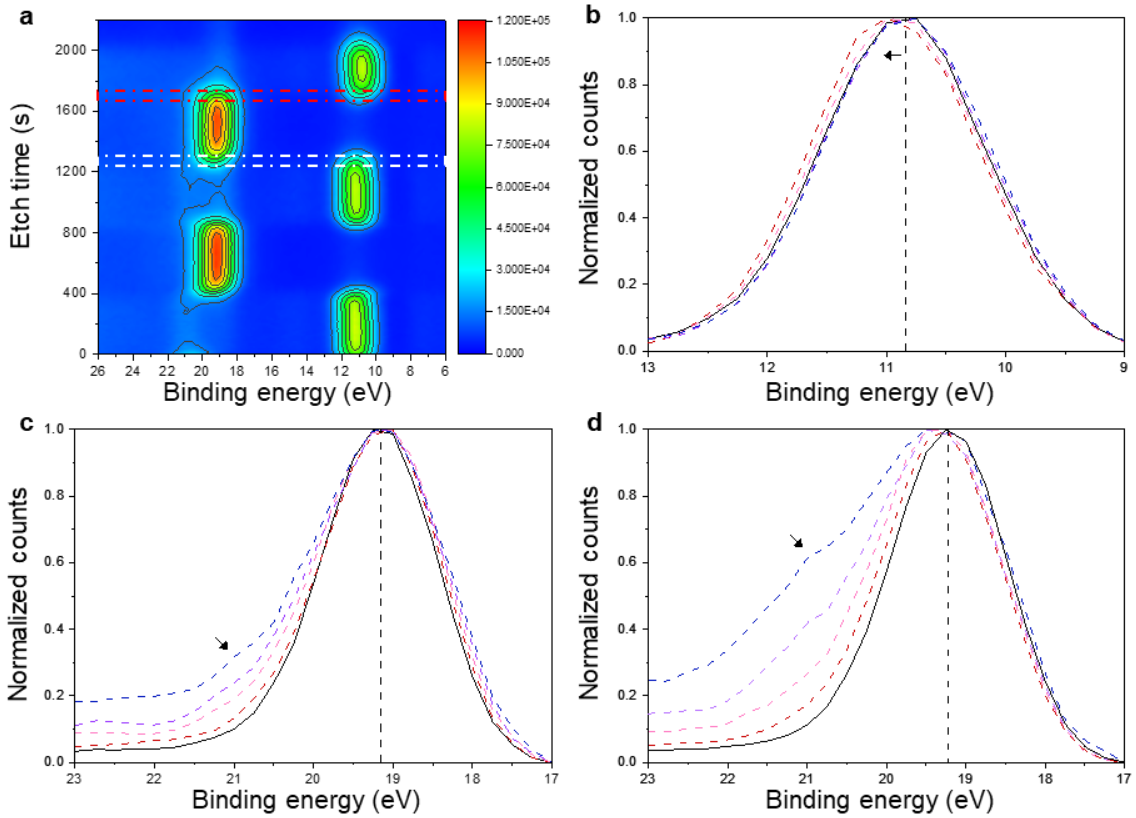

s

Figure 4. (a) Two-dimensional contour map of the depth-resolved XPS spectra for Z/G-4 in the energy region of the Zn 3d and Ga 3d peaks. (b) XPS spectra in the energy region of the Zn 3d peak near the interface closest to the substrate (i.e. the region indicated by the red dotted lines in (a)). (c) XPS spectra in the energy region of the Ga 3d peak near the interface closest to the substrate. (d) XPS spectra in the energy region of the Ga 3d peak near the 2nd interface from the substrate (i.e. the region indicated by the white dotted lines in (a)). In (b-d), the blue lines indicate the spectra acquired on the ZnS side of the interface and red lines indicate the spectra acquired on the GaP side of the interface; the color scale transitions from

blue to red indicating position at which the spectra was acquired going from the ZnS to the GaP side of the interface. The black lines are the spectra acquired in the bulk material away from the interface (on the ZnS side for (b), and on the GaP side for (c) and (d)).

In summary, the XPS results confirm the DFT prediction that there are electronic states associated with atomic bonding environments at the ZnS-GaP interfaces and that these electronic states can result in a band gap reduction. It is this band gap reduction that leads to the observed visible-light photocurrent that has been attributed to the effect of the interfaces.

4. CONCLUSIONS

We have presented a new non-oxide photoelectrode material and shown enhancement of the photocurrent density under visible light due to the presence of ZnS/GaP interfaces in multilayered films. The activity extends to long wavelengths (650 nm). Consistent with these findings, DFT calculations indicate the formation of electronic states associated with atomic bonding environments at the interfaces between ZnS and GaP films that are different from the states for atoms away from the interfaces; these interfacial electronic states can lead to a local reduction in the band gap. The introduction of these electronic states associated with the interfaces has been confirmed by depth-resolved XPS. Overall, this work demonstrates the ability to use interfaces *between* materials, rather than changes to bulk materials, to control light absorption and hence achieve visible-light photoactivity.

SUPPORTING INFORMATION

High resolution transmission electron microscopy (HRTEM) cross-section images, (111) peak from XRD patterns, Ga 3d XPS peak near the two outer interfaces of the Z/G-4 film are included in the supporting information.

ACKNOWLEDGEMENTS

This work was supported by the Australian Research Council (ARC) Discovery Projects scheme and the Science, Technology and Innovation Commission of Shenzhen Municipality (Grant No. KQTD20160226195659991). This research used the facilities supported by Australian Microscopy & Microanalysis Research Facility at the Electron Microscope Unit at UNSW. This research was undertaken with the assistance of computational resources provided by the Australian Government through the National Computational Infrastructure (NCI) under the National Computational Merit Allocation Scheme. This research was supported by an Australian Government Research Training Program (RTP) Scholarship.

AUTHOR CONTRIBUTIONS

CKP fabricated the films and performed all physical characterisation, except TEM, and PEC measurements. PSMG performed the HRTEM, with assistance from XL and JH. CT and YHN assisted with planning and interpreting the PEC measurements. MA.-F. and JNH performed the calculations, with advice and help in interpretation from NLA. FK developed the experimental plan. JNH, NV and YHN supervised the work. All authors contributed to the manuscript preparation.

REFERENCES

(1) Kudo, A. & Miseki, Y. Heterogeneous Photocatalyst Materials for Water Splitting. *Chem. Soc. Rev.* **2009,** *38*, 253–278.

(2) Zhang, K.; Ma, M.; Li, P.; Wang, D. H. & Park, J. H. Water Splitting Progress in Tandem Devices: Moving Photolysis Beyond Electrolysis. *Advanced Energy Materials* **2016,** *6*, 1600602.

(3) Osterloh, F. E. Inorganic Materials as Catalysts for Photochemical Splitting of Water. *Chemistry of Materials* **2008,** *20*, 35–54.

(4) Maeda, K. & Domen, K. New Non-Oxide Photocatalysts Designed for Overall Water Splitting under Visible Light. *The Journal of Physical Chemistry C* **2007,** *111*, 7851–7861.

(5) Scaife, D. Oxide Semiconductors in Photoelectrochemical Conversion of Solar Energy. *Solar Energy* **1980,** *25*, 41–54.

(6) Maeda, K. & Domen, K. Photocatalytic Water Splitting: Recent Progress and Future Challenges. *The Journal of Physical Chemistry Letters* **2010,** *1*, 2655–2661.

(7) Hisatomi, T.; Kubota, J. & Domen, K. Recent Advances in Semiconductors for Photocatalytic and Photoelectrochemical Water Splitting. *Chem. Soc. Rev.* **2014,** *43*, 7520–7535.

(8) Li, X.; Yu, J.; Low, J.; Fang, Y.; Xiao, J.; Chen, X. Engineering Heterogeneous Semiconductors for Solar Water Splitting. *Journal of Materials Chemistry A* **2015,** *3*, 2485–2534.

(9) Murashkina, A. A.; Murzin, P. D.; Rudakova, A. V.; Ryabchuk, V. K.; Emeline, A. V.; Bahnemann, D. W. Influence of the Dopant Concentration on the Photocatalytic Activity: Al-Doped TiO_2. *The Journal of Physical Chemistry C* **2015,** *119*, 24695–24703.

(10) Kay, A.; Grave, D. A.; Ellis, D. S.; Dotan, H.; Rothschild, A. Heterogeneous Doping to Improve the Performance of Thin-Film Hematite Photoanodes for Solar Water Splitting. *ACS Energy Letters* **2016,** *1*, 827–833.

(11) Ge, J.; Yu, Y.; Yan, Y. Earth-Abundant Orthorhombic $BaCu_2Sn(Se_xS_{1-x})4$ ($x \approx 0.83$) Thin Film for Solar Energy Conversion. *ACS Energy Letters* **2016,** *1*, 583–588.

(12) Muñoz-Batista, M. J.; Gómez-Cerezo, M. N.; Kubacka, A.; Tudela, D.; Fernández-García, M. Role of Interface Contact in CeO_2–TiO_2 Photocatalytic Composite Materials. *ACS Catalysis* **2013,** *4*, 63–72.

(13) Hwang, H. Y. Atomic Control of the Electronic Structure at Complex Oxide Heterointerfaces. *MRS Bulletin* **2006,** *31*, 28–35.

(14) Schlom, D. G.; Chen, L. Q.; Pan, X.; Schmehl, A. & Zurbuchen, M. A. A Thin Film Approach to Engineering Functionality into Oxides. *Journal of the American Ceramic Society* **2008,** *91*, 9429–2454.

(15) Moniz, S. J. A.; Shevlin, S. A.; Martin, D. J.; Guo, Z.-X. & Tang, J. Visible-Light Driven Heterojunction Photocatalysts for Water Splitting – A Critical Review. *Energy & Environmental Science* **2015,** *8*, 731–759.

(16) Graetzel, M.; Janssen, R. A. J.; Mitzi, D. B. & Sargent, E. H. Materials Interface Engineering for Solution-Processed Photovoltaics. *Nature* **2012,** *488*, 304–312.

(17) Zhang, Z.; Wang, W.; Wang, L.; Sun, S. Enhancement of Visible-Light Photocatalysis by Coupling with Narrow-Band-Gap Semiconductor: A Case Study on Bi_2S_3/Bi_2WO_6. *ACS Applied Materials & Interfaces* **2012,** *4*, 593–597.

(18) Zhang, Y. C.; Du, Z. N.; Li, K. W.; Zhang, M.; Dionysiou, D. D. High-Performance Visible-Light-Driven SnS_2/SnO_2 Nanocomposite Photocatalyst Prepared via In Situ Hydrothermal Oxidation of SnS_2 Nanoparticles. *ACS Applied Materials & Interfaces* **2011,** *3*, 1528–1537.

(19) Standing, A.; Assali, S.; Gao, L.; Verheijen, M. A.; Dam, D. V.; Cui, Y.; Notten, P. H. L.; Haverkort, J. E. M.; Bakkers, E. P. A. M. Efficient Water Reduction with Gallium Phosphide Nanowires. *Nature Communications* **2015,** *6*, 7824.

(20) Kamimura, S.; Beppu, N.; Sasaki, Y.; Tsubota, T. & Ohno, T. Platinum and Indium Sulfide-Modified Cu_3BiS_3 Photocathode for Photoelectrochemical Hydrogen Evolution. *Journal of Materials Chemistry A* **2017,** *5*, 10450–10456.

(21) May, M. M.; Lewerenz, H.-J.; Lackner, D.; Dimroth, F. & Hannappel, T. Efficient Direct Solar-to-Hydrogen Conversion by In Situ Interface Transformation of a Tandem Structure. *Nature Communications* **2015,** *6*, 8286.

(22) Gu, J.; Yan, Y.; Young, J. L.; Steirer, K. X.; Neale, N. R.; Turner, J. A. Water Reduction By a p-$GaInP_2$ Photoelectrode Stabilized by an Amorphous TiO_2 Coating and a Molecular Cobalt Catalyst. *Nature Materials* **2015,** *15*, 456–460.

(23) Hu, S.; Shaner, M. R.; Beardslee, J. A.; Lichterman, M.; Brunschwig, B. S.; Lewis, N. S. Amorphous TiO_2 Coatings Stabilize Si, GaAs, and GaP Photoanodes for Efficient Water Oxidation. *Science* **2014,** *344*, 1005–1009.

(24) Hart, J. N. & Allan, N. L. GaP-ZnS Solid Solutions: Semiconductors for Efficient Visible Light Absorption and Emission. *Advanced Materials* **2013,** *25*, 2989–2993.

(25) Strandwitz, N. C.; Turner-Evans, D. B.; Tamboli, A. C.; Chen, C. T.; Atwater, H. A.; Lewis, N. S. Photoelectrochemical Behavior of Planar and Microwire-Array Si|GaP Electrodes. *Advanced Energy Materials* **2012,** *2*, 1109–1116.

(26) Park, K.; Lee, J. A.; Im, H. S.; Jung, C. S.; Kim, H. S.; Park, J.; Lee, C.-L. GaP–ZnS Pseudobinary Alloy Nanowires. *Nano Letters* **2014,** *14*, 5912–5919.

(27) Maeda, K.; Teramura, K. & Domen, K. Effect of Post-Calcination on Photocatalytic Activity of $(Ga_{1-x}Zn_x)(N_{1-x}O_x)$ Solid Solution for Overall Water Splitting Under Visible Light. *Journal of Catalysis* **2008,** *254*, 198–204.

(28) Dovesi, R.; Saunders, V. R.; Roetti, C.; Orlando, R.; Zicovich-Wilson, C. M.; Pascale, F.; Civalleri, B.; Doll, K.; Harrison, N. M.; Bush, I. J. *et al.* CRYSTAL14 User's Manual (University of Torino, Torino, 2014).

(29) Dovesi, R.; Orlando, R.; Erba, A.; Zicovich-Wilson, C. M.; Civalleri, B.; Casassa, S.; Maschio, L.; Ferrabone, M.; Pierre, M. D. L.; Darco, P.; Noël, Y. *et al*. CRYSTAL14: A Program for the *ab initio* Investigation of Crystalline Solids. *Int. J. Quantum Chem.* **2014,** *114*, 1287–1317.

(30) Jaffe, J. E. & Hess, A. C. Hartree-Fock Study of Phase Changes in ZnO at High Pressure. *Physical Review B* **1993,** *48*, 7903–7909.

(31) Lichanot, A.; Aprà, E. & Dovesi, R. Quantum Mechanical Hartree-Fock Study of the Elastic Properties of Li_2S and Na_2S. *Physica Status Solidi (b)* **1993,** *177*, 157–163.

(32) Causà, M.; Dovesi, R. & Roetti, C. Pseudopotential Hartree-Fock Study of Seventeen III-V and IV-IV Semiconductors. *Physical Review B* **1991,** *43*, 11937–11943.

(33) Becke, A. D. Density-Functional Thermochemistry. III. The Role of Exact Exchange. *The Journal of Chemical Physics* **1993,** *98*, 5648–5652.

(34) Perdew, J. P. & Wang, Y. Accurate and Simple Analytic Representation of the Electron-Gas Correlation Energy. *Physical Review B* **1992,** *45*, 13244–13249.

(35) Malizia, M.; Seger, B.; Chorkendorff, I. & Vesborg, P. C. K. Formation of a p-n Heterojunction on GaP Photocathodes for H_2 Production Providing an Open-Circuit Voltage of 710 mV. *J. Mater. Chem. A* **2014,** *2*, 6847–6853.

(36) Parameshwaran, V.; Xu, X. & Clemens, B. Electrochemical Reduction Properties of Extended Space Charge InGaP and GaP Epitaxial Layers. *Journal of The Electrochemical Society* **2016,** *163*, H714–H721.

(37) Price, M. J. & Maldonado, S. Macroporous n-GaP in Nonaqueous Regenerative Photoelectrochemical Cells. *The Journal of Physical Chemistry C* **2009,** *113*, 11988–11994.

(38) Maeda, K.; Teramura, K.; Lu, D.; Takata, T.; Saito, N.; Inoue, Y.; Domen, K. Photocatalyst Releasing Hydrogen from Water. *Nature* **2006,** *440*, 295–295.

(39) Cheng, H.-E.; Lee, W.-J.; Hsu, C.-M.; Hon, M.-H. & Huang, C.-L. Visible Light Activity of Nitrogen-Doped TiO_2 Thin Films Grown by Atomic Layer Deposition. *Electrochemical and Solid-State Letters* **2008,** *11*, D81–D84.

(40) Wang, C.; Chen, Z.; Jin, H.; Cao, C.; Li, J.; Mi, Z. Enhancing Visible-Light Photoelectrochemical Water Splitting Through Transition-Metal Doped TiO_2 Nanorod Arrays. *J. Mater. Chem. A* **2014,** *2*, 17820–17827.

(41) Kim, T. W.; Ping, Y.; Galli, G. A. & Choi, K.-S. Simultaneous Enhancements in Photon Absorption and Charge Transport of Bismuth Vanadate Photoanodes for Solar Water Splitting. *Nature Communications* **2015,** *6*, 8769.

(42) Haynes, W. M. & Lide, D. R. CRC Handbook of Chemistry and Physics: A Ready-Reference Book of Chemical and Physical Data. (CRC Press, 2011).
(43) Ley, L.; Pollak, R. A.; Mcfeely, F. R.; Kowalczyk, S. P.; Shirley, D. A. Total Valence-Band Densities of States of III-V and II-VI Compounds from X-Ray Photoemission Spectroscopy. *Physical Review B* **1974,** *9*, 600–621.
(44) Leonhardt, G.; Berndtsson, A.; Hedman, J.; Klasson, M.; Nilsson, R.; Nordling, C. ESCA Studies of Some $A^{III}B^{V}$ Compounds with Ga and As. *Physica Status Solidi (b)* **1973,** *60*, 241–248.

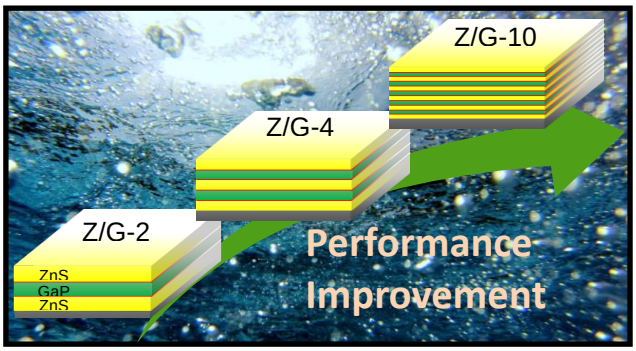

“TOC Graphic”